Journal of Marine Research, 58, 789–808, 2000

Water-mass formation and potential vorticity balance in an abyssal ocean circulation

by Jiayan Yang[1] and James F. Price[1]

ABSTRACT

Our goal is to develop some understanding and intuition regarding abyssal ocean circulations. To do this we investigate highly idealized, source/sink-driven flows computed by a single layer, numerical ocean model forced by a prescribed source or sink. The interior circulation is always found to be very slow and Stommel-Arons like. On the other hand, the intense boundary currents may vary considerably from case to case, depending largely upon the potential vorticity (PV) associated with the source or sink. If the source is imposed by downwelling along a northern boundary, then the associated PV flux is zero, and the resulting steady circulation can induce no net frictional torque. The result is a rather complex pattern of boundary layer flow that includes a strong recirculation along the northern boundary. If the same mass flux is injected as a laminar, horizontal inflow, then the associated PV flux is significant, and must be balanced in steady state by frictional torque. The result is a unidirectional boundary layer flow away from the source. Other experiments elucidate the effect of vortex stretching on topography. For example, a horizontal outflow over shallowing topography induces a net cyclonic frictional torque in the boundary layer circulation of the basin. An understanding of the steady state PV balance thus appears to confer some insight into the form of boundary layer flows in these abyssal circulations.

1. Introduction

The vast water mass that fills the deep ocean is uniformly cold, indicating an origin in polar or subpolar regions where dense water is formed by air-sea interaction. The cold source water is carried to lower-latitudes mainly via western boundary currents and returned to the surface layer by upwelling in the ocean interior (Warren, 1981). The development of the modern theory of this abyssal ocean circulation began with the remarkable work of Stommel (1958) and Stommel and Arons (1960a,b) (reviewed recently by Pedlosky, 1996). The Stommel-Arons theory assumes that the water mass return occurs over a very broad scale by upwelling. It then applies the Sverdrup balance to link the interior circulation with vortex stretching induced by the upwelling. The Stommel-Arons theory concludes that a southward flowing western-boundary current must exist in order to carry water away from a northern source and to supply water to the ocean interior.

1. Department of Physical Oceanography, Woods Hole Oceanographic Institution, Woods Hole, Massachusetts, 02543, U.S.A. ***email: jyang@whoi.edu;jprice@whoi.edu***

In this paper we consider some qualitative aspects of such source-driven abyssal circulations. Our starting point is the recognition that there are different ways in which source water can be introduced into the abyssal ocean, either by downwelling associated with free, open ocean convection, or by a nearly horizontal inflow through a side boundary. The former process occurs, for example, in the Labrador Sea production of upper North Atlantic Deep Water (NADW), and the latter process is an idealized model of the outflow of lower North Atlantic Deep Water through Denmark Strait or Faroe Bank Channel into the North Atlantic. The question we address here is—Does it matter which source, downwelling or convection, supplies deep water to an ocean basin?

We cannot point to observations adequate to address this question. The immediate motivation is instead that most ocean GCMs produce deep water by open ocean convection, simply because northern marginal seas are often omitted or are not represented with enough resolution to permit realistic overflows. The question we can directly answer is, How does the omission of marginal sea overflows affect the abyssal circulation of OGCMs? In practice we will consider that inflow processes occur in isolation, and within a highly idealized ocean basin having very simple bottom relief and with no wind-driven circulation. It should be apparent, then, that this is a study of highly idealized models rather than of the real ocean. Our goal is to develop intuition for abyssal circulations, and not to simulate a specific circulation. There is, however, fairly obvious geophysical motivation for most of the experiments that follow.

In the next section, the results from a pair of numerical experiments will be presented to demonstrate the difference in abyssal circulation resulting from different types of water-mass source. The change in the form of the circulation will be explained in terms of the PV budget. Results from some additional linear model experiments are presented in Section 3. Some effects of topography will be examined in Section 4. A summary is given in Section 5.

2. A simple model of source-driven abyssal circulation

a. Model dynamics

Our purpose is to investigate whether and how the abyssal circulation is affected by the form of a specified water-mass source. We address this issue by using the simplest possible model that is adequate in simulating a Stommel-Arons's-type source-sink driven circulation—a reduced-gravity model governed by the momentum and continuity equations:

$$\frac{Du}{Dt} - fv + g' \frac{\partial h}{\partial x} = -\lambda u \tag{1}$$

$$\frac{Dv}{Dt} + fu + g' \frac{\partial h}{\partial y} = -\lambda v \tag{2}$$

$$\frac{Dh}{Dt} + (H + h)\left(\frac{\partial u}{\partial x} + \frac{\partial v}{\partial y}\right) = Q - \kappa h \tag{3}$$

where D/Dt is the rate of change following the fluid, Q is a prescribed water-mass source inside the basin (this will be zero in cases having an overflow source through a side boundary), H and h are the mean and the deviation of the layer thickness with $h \ll H$, $g' = \Delta\rho g/\rho_0$ is the reduced gravity, and $\lambda = 1/(8.5 \text{ days})$ and $\kappa = 1/(200 \text{ days})$ are the damping coefficients. This model is very similar to that of Kawase (1987) except that we allow momentum advection for reasons described below. A difference between this model and the Stommel-Arons model is that the upwelling velocity, represented by the last term in (3), is linked to the model dynamics rather than being prescribed as uniform. The form and even the existence of this thickness damping term is of secondary importance here. Rayleigh damping of momentum as it appears here leads to particularly simple diagnostics of vorticity balance. However, our understanding of the processes that cause frictional dissipation in such circulations is rudimentary, at best, and so we emphasize qualitative features of the circulation that are not unduly sensitive to the form of dissipation.

Following Kawase (1987), the spherical coordinate version of (1)–(3) is used in the numerical code. The Rossby deformation radius is about 61 km at 40° in latitude and about 500 km at the equator. The model extends from 40S to 40N and spans 40° zonally. The model resolution is $\theta = 0.5°$ and $\phi = 0.25°$, and the staggered Arakawa-C grid is used. We used $g' = 0.0129 \text{ m s}^{-2}$ and $H = 2500$ m for all the flat-bottom runs, which give an equivalent depth of 3.3 m. The condition of no normal flow is applied at the solid boundary. The model is spun up to an equilibrium state from an initial condition of no motion by a water-mass source of 1 Sv. This mass flux gives a basin-averaged upwelling velocity of about $\overline{w} = 2.8 \times 10^{-8} \text{ m s}^{-1}$, and an averaged layer-thickness deviation of about $\overline{h} = \overline{w}/\kappa = 0.48$ m.

b. *Numerical experiments*

Two parallel experiments are considered. In the first one, the water-mass is introduced inside the basin through Q in (3) and all side boundaries are closed. This is referred to as the *closed-basin model.* In the second experiment, the inside-basin source Q in (3) is turned off, and the water mass is introduced as a flow across a side boundary. This case is denoted as the *open-basin model.* The linear version of (1)–(3) is used in these experiments for an idealized basin with a flat bottom ($H = 2500$ m).

In the first closed-basin experiment, a downwelling water-mass source Q is specified to be in a northeastern area, bounded by $34° \le \phi \le 38°$ and $34\text{N} \le \theta \le 38\text{N}$, as indicated in Figure 1(b). The layer-thickness deviation and the transport velocity $H\mathbf{u}$ in the equilibrium state are shown in Figure 1(a)–(b). The velocity along the western and northern boundaries is much greater than in the interior, and the transport vector plotted in Figure 1(b) is truncated at $0.5 \text{ m}^2 \text{ s}^{-1}$ in order to show the basin-wide flow field. A striking feature in this solution is a strong anticyclonic gyre between 30 and 40N that is associated with a strong eastward flow along the northern boundary. Outside this gyre, the circulation consists of a western boundary current that transports water mass to the rest of the basin where the upwelling in the interior drives poleward flow consistent with the expected linear PV balance of the Stommel-Arons model.

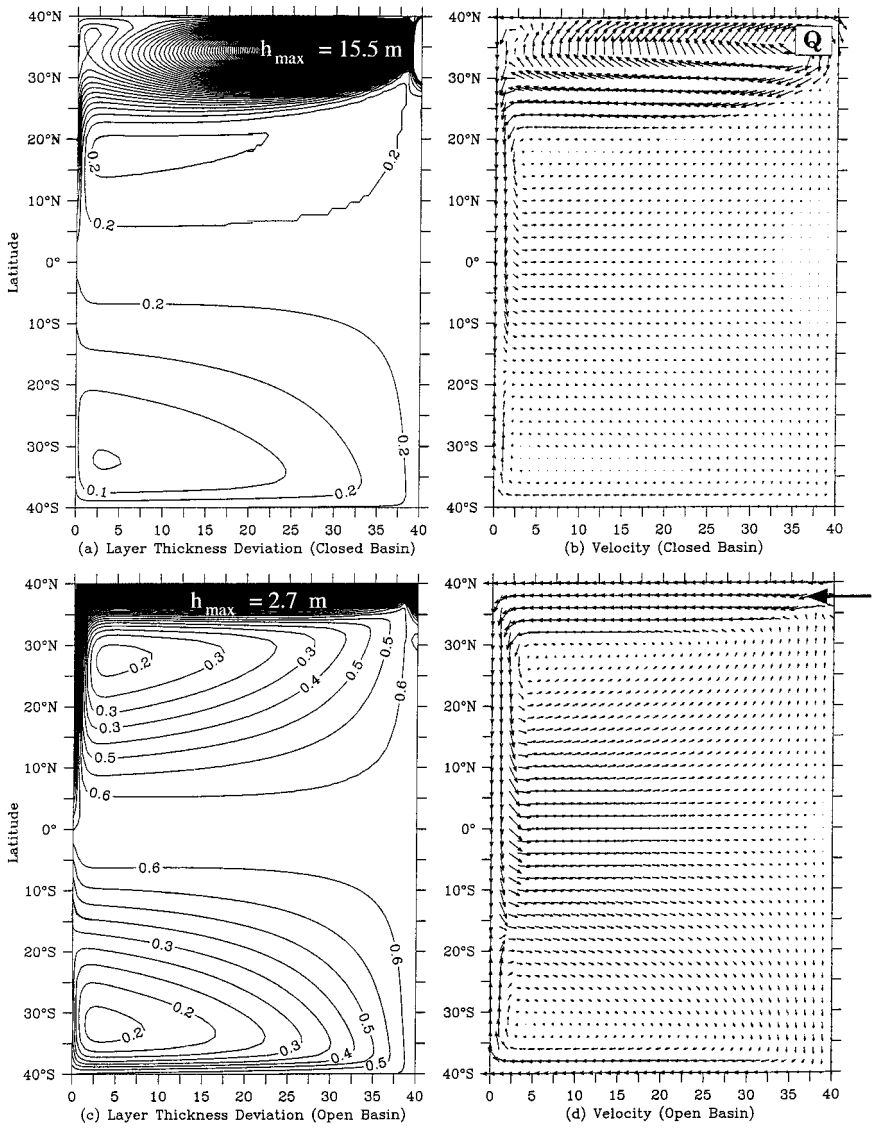

Figure 1. (a) The deviation of the layer thickness and (b) the circulation field in a closed-basin run in which a water-mass source Q of 1 Sv is placed inside the box near the northeastern corner. The transport velocity Hu is truncated at 0.5 $m^2\ s^{-2}$ in order to show the weak interior flow. (c)–(d) are the same as (a)–(b) except from the 'open-basin' model where the inflow is indicted by the arrow. The major difference of these two experiments is the existence of a strong recirculation and the reversal of the northern boundary current in the closed-basin case.

In the companion 'open-basin' experiment, the water-mass source is specified as a zonal inflow across the eastern boundary at the northeastern corner in the model. Except for this difference in the water-mass source, the model is the same as before. The pattern and the magnitude of the circulation appear to be very different from what was found in the closed-basin case (compare Figs 1(a)–(b) and 1(c)–(d)), particularly the strength and direction of these boundary currents. The along-boundary current, started from the northwestern corner of the model domain, is plotted in Figure 2(a) (positive for counter-clockwise direction). The strength of the western-boundary current is much greater in the open-basin model (solid line), and the direction of the northern-boundary current is just opposite that found in the closed-basin model. How can we understand the difference in these two cases?

c. Vorticity budget

We can make significant progress toward understanding these circulations by understanding their vorticity balance. Assuming that a flat-bottom basin is filled with incompressible and stratified fluid, then the vorticity equation (Pedlosky, 1979; Rhines, 1983) can be written as:

$$\frac{D}{Dt}(\nabla \times \mathbf{u} + 2\Omega) = ((\nabla \times \mathbf{u} + 2\Omega) \cdot \nabla)\mathbf{u} - \lambda \nabla \times \mathbf{u} \tag{4}$$

where $\mathbf{u} = (u, v, w)$ is the velocity vector, Ω is the earth's rotation vector, and λ is the Rayleigh friction coefficient.

The vertical component of the vorticity in a steady state is governed by:

$$\mathbf{u} \cdot \nabla(f + \zeta) = (f + \zeta)\frac{\partial w}{\partial z} - \lambda\zeta \tag{5}$$

where relative vorticity $\zeta = v_x - u_y$. This is a familiar vorticity equation which states that the balance is among vorticity advection, vortex stretching and friction. In general, all three terms are important, and little more can be said regarding the local balance.

A more useful two term balance arises upon taking the basin integral. To derive that we first rewrite the advection term in flux form by using $\nabla \cdot \mathbf{u} = 0$, so that (5) becomes

$$\nabla \cdot [\mathbf{u}(f + \zeta)] = (f + \zeta)\frac{\partial w}{\partial z} - \lambda\zeta, \tag{6}$$

and separating the divergence term on the left-hand side into the horizontal and vertical components yields:

$$\nabla \cdot [\mathbf{u}_h(f + \zeta)] + \underbrace{\frac{\partial}{\partial z}[w(f + \zeta)]}_{A_1} = \underbrace{(f + \zeta)\frac{\partial w}{\partial z}}_{A_2} - \lambda\zeta \tag{7}$$

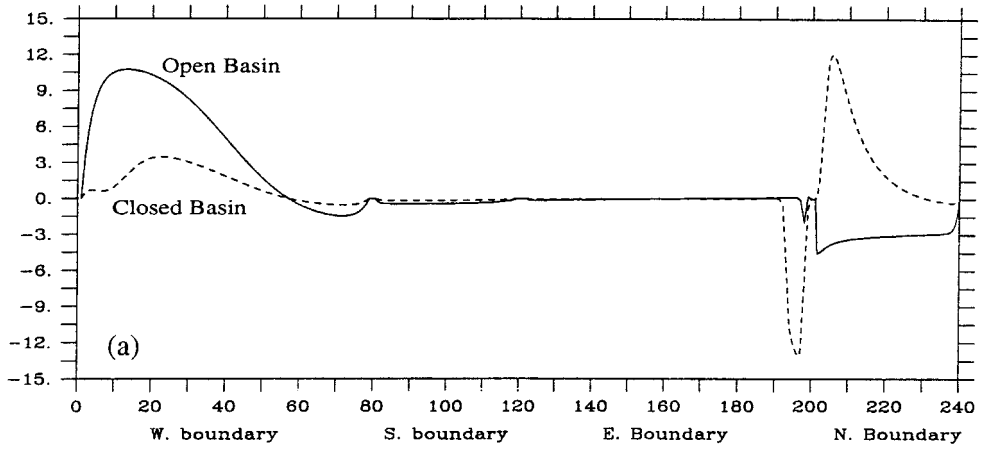

(a) The velocity along the boundary.

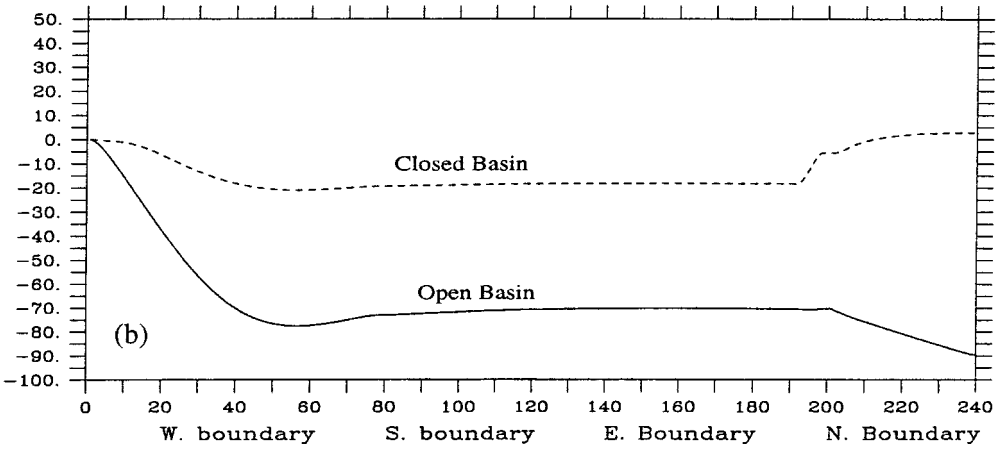

(b) The accumulated frictional vorticity production F(s).

Figure 2. (a) The velocity along all four boundaries (anticlockwise starting at the northwestern corner) in both the closed-basin (dashed) and open-basin (solid) cases, (b) the accumulated frictional vorticity production $F(s)$ by the boundary current (see the definition in (16)). The vorticity production by friction, $F(s)$, calculated from the model results agrees very well with that expected from the constraints (14) and (15).

where $\mathbf{u}_h = (u, v)$ is the horizontal velocity vector. The terms A_1 and A_2 are in a similar form, but they arise from distinct physical processes. A_1 is the vorticity transport associated with the vertical mass-flux, while A_2 is the local vorticity production due to vortex stretching. For the linear dynamics, these two terms are identical because f is independent

of the depth, and, therefore, a vertical velocity w does not contribute to the vorticity budget. To see this, consider a downwelling of water mass into an abyssal layer. Downwelling brings positive planetary vorticity into the layer in the northern hemisphere (A_1), but it also squashes vortex lines so that negative vorticity is produced locally (A_2). This negative vorticity production erases the planetary vorticity brought into the layer by the water-mass source, and thus A_1 and A_2 cancel. In the nonlinear case, these two terms do not necessarily cancel each other exactly if the adjacent layers have different relative vorticity ζ. However, the difference between A_1 and A_2 is usually very small because f is typically much greater than ζ for large-scale flows, and (7) can be well approximated as:

$$\nabla \cdot [\mathbf{u}_h(f + \zeta)] = -\lambda\zeta. \tag{8}$$

Integrating over the entire basin and employing the divergence and Stokes theorems (e.g., Pedlosky, 1996) gives

$$\oint_C (\mathbf{u}_h \cdot \mathbf{n})(f + \zeta)\, ds = -\lambda \oint_C (\mathbf{u}_h \cdot \mathbf{l})\, ds \tag{9}$$

where $\mathbf{n}$ and $\mathbf{l}$ are unit vectors perpendicular and tangential to the lateral boundary, respectively.

We also consider an abyssal layer with a thickness of $H(x, y)$ overlying the bottom topography $D(x, y)$. For flows undergoing significant expansion/contraction of layer thickness, such as over a sill, it is more useful to use depth-integrated rather than depth-averaged variables. Because all variables are assumed to be depth-independent within the layer, Eq. (8) can be re-written as:

$$\nabla \cdot \int_D^{D+H+h} \mathbf{u}_h \left(\frac{f + \zeta}{H + h}\right) dz = -\lambda \int_D^{D+H+h} \left(\frac{\zeta}{H + h}\right) dz$$

or

$$\nabla \cdot \left[\mathbf{U}_h \left(\frac{f + \zeta}{H + h}\right)\right] = -\lambda \left(\frac{\zeta}{H + h}\right)(H + h) = -\lambda\zeta \tag{10}$$

where $U_h = u_h(H + h)$ is the depth-integrated transport velocity, and $(f + \zeta)/(H + h) = PV$ is the potential vorticity. To examine the PV budget, we integrate (10) over the whole basin S,

$$\int\int_S \nabla \cdot \left[\mathbf{U}_h \left(\frac{f + \zeta}{H + h}\right)\right] dxdy = -\int\int_S \lambda\zeta\, dxdy,$$

and again convert to a line integral along the side boundary C,

$$\oint_C (\mathbf{U}_h \cdot \mathbf{n}) \left(\frac{f + \zeta}{H + h}\right) ds = -\lambda \oint_C (\mathbf{u}_h \cdot \mathbf{l})\, ds. \tag{11}$$

Assuming that the basin has N openings along the boundary at $s1_i \le s_i \le s2_i$ ($i = 1, 2, \ldots, N$),

the PV constraint (11) becomes:

$$\sum_{i=1}^{N} \int_{s1_i}^{s2_i} (\mathbf{U}_h \cdot \mathbf{n}) \left(\frac{f+\zeta}{H+h} \right) ds = -\lambda \oint_C (\mathbf{u}_h \cdot \mathbf{l})\, ds. \tag{12}$$

The transport of relative vorticity at an opening can be further simplified to:

$$\int_{s1_i}^{s2_i} (\mathbf{U}_h \cdot \mathbf{n}) \frac{\zeta}{H+h} ds = \int_{s1_i}^{s2_i} (\mathbf{u}_h \cdot \mathbf{n}) \zeta \, ds = \frac{1}{2} \left[(\mathbf{u}_h \cdot \mathbf{n})^2 \big|_{s=s2_i} - (\mathbf{u}_h \cdot \mathbf{n})^2 \big|_{s=s1_i} \right]$$

where $(\mathbf{u}_h \cdot \mathbf{n})\big|_{s=s1_i, s2_i}$ are velocity directed into the basin at the two sides of the opening. In the case of a slug flow this advection term vanishes. It would vanish generally if no-slip conditions bring the inflow current to zero at the sides of an inflow channel. Thus a unidirectional, steady inflow would be expected to transport zero relative vorticity into the basin and (12) becomes,

$$\sum_{i=1}^{N} \int_{s1_i}^{s2_i} (\mathbf{U}_h \cdot \mathbf{n}) \frac{f}{H+h} ds = -\lambda \oint_C (\mathbf{u}_h \cdot \mathbf{l})\, ds. \tag{13}$$

If $h \ll H$ and the variation of H across the opening is small, this integral constraint can be further simplified to

$$\sum_{i=1}^{N} \frac{Q_i f_i}{H_i} = -\lambda \oint_C (\mathbf{u}_h \cdot \mathbf{l})\, ds, \tag{14}$$

where Q_i is the volume transport out of the basin across $s1_i \le s_i \le s2_i$, and f_i and H_i are the Coriolis parameter and the mean layer thickness at the i-th opening. Eq. (14) indicates that in steady state, *the PV inflow across the side boundary into a density layer is balanced by the net PV dissipation within this layer.* It should be pointed out that (14) also applies to an intermediate case in which the water-mass flux into the layer is supplied by both vertical velocity and a side-boundary inflow. The integral (14) applies to the linear model as well, such as that shown in Figure 1, where the relative *PV* transport was neglected by the assumption of linearity and H variability was negligible.

3. Discussion of model results

a. Linear model

The major difference between the parallel experiments of Section 2(b) is the existence of a recirculation gyre and the reversal of the northern-boundary current in the 'closed-basin' model (Fig. 1(a)–(b)) as compared with the 'open-basin' model (Fig. 1(c)–(d)). In the former case, the vorticity source vanishes, and thus the vorticity production by friction (the right-hand side in (14)) must vanish, i.e.,

$$\lambda \oint_C (\mathbf{u} \cdot \mathbf{l})\, ds = 0 \tag{15}$$

and thus the integral of the tangential velocity along the boundary must vanish. A reversal of the northern-boundary current is thus required in order to counter-balance the mostly southward western-boundary current so that (15) can be satisfied. In the 'open-basin' model, the *PV* constraint (14) requires that the Rayleigh friction produces a sufficient amount of negative (clockwise) *PV* to balance the inflow of planetary *PV*. Therefore, a strong counterclockwise boundary current is developed along the northern and most of the western boundary. The qualitative difference in these two circulation fields can thus be understood as a consequence of the two different water mass and *PV* sources. To show this result quantitatively, we calculate the 'accumulated' frictional *PV* production by the boundary current, starting from $s = 0$ at the northwestern corner and integrating anticlockwise along the boundary to a location s, i.e.,

$$F(s) = -\lambda \int_0^s (\mathbf{u} \cdot \mathbf{l})\, ds. \tag{16}$$

For the closed-basin case, the integral $F(s)$ must return to zero after integration along all four boundaries. For the open-basin case, the $F(s)$ value after completing the integration must equal the inflow of the planetary vorticity. We use a free-slip boundary condition to infer the tangential velocity at the side boundary. Figure 2(b) shows $F(s)$ along all side boundaries for both the closed-basin (dashed line) and open-basin (solid line) cases. The $F(s)$ value at the end of integration is about 2.5 $m^2\ s^{-2}$ (as compared with the theoretical value of 0 $m^2\ s^{-2}$) for the closed-basin model and about -90 $m^2\ s^{-2}$ (as compared with -91.5 $m^2\ s^{-2}$ for the specified planetary-vorticity inflow) for the open-basin model. Thus the constraints (14) and (15) are satisfied to within a few percent accuracy in the numerical solutions.

The particularly simple result that the net frictional torque is proportional to the line integral of current along the boundary is a consequence of the Rayleigh friction law. We have tried much smaller values of parameter λ, which might be more realistic. The pattern of the circulation is exactly the same, though the width of the boundary current shrinks as expected. We have also tried lateral diffusion in place of Rayleigh friction, and again the pattern of the circulation is little altered. To that extent, we believe that the qualitative features of the boundary-layer circulation emphasized here are due more to the vorticity source than to the poorly known frictional parameterization.

i. Northwestern source. In the next experiments, the water-mass source is moved to the northwestern corner between $\theta = 34$N and $\theta = 39$N and $\phi = 1°$ and $\phi = 3°$, Figure 3(a)–(b). These results are basically identical to what was shown in Kawase's paper except for the amplitude difference due to the different forcing strength (1 Sv in our model). As before, the transport velocity is truncated at the level of 0.5 $m^2\ s^{-1}$ in Figure 3(b). The real boundary current, especially near the water-mass source, is thus much greater than what appears in Figure 3(b). This is clearly shown in Figure 4(a) which plots the along-boundary current velocity, starting from the northwestern corner and going anticlockwise (dashed line for the closed basin). The maximum northward velocity along

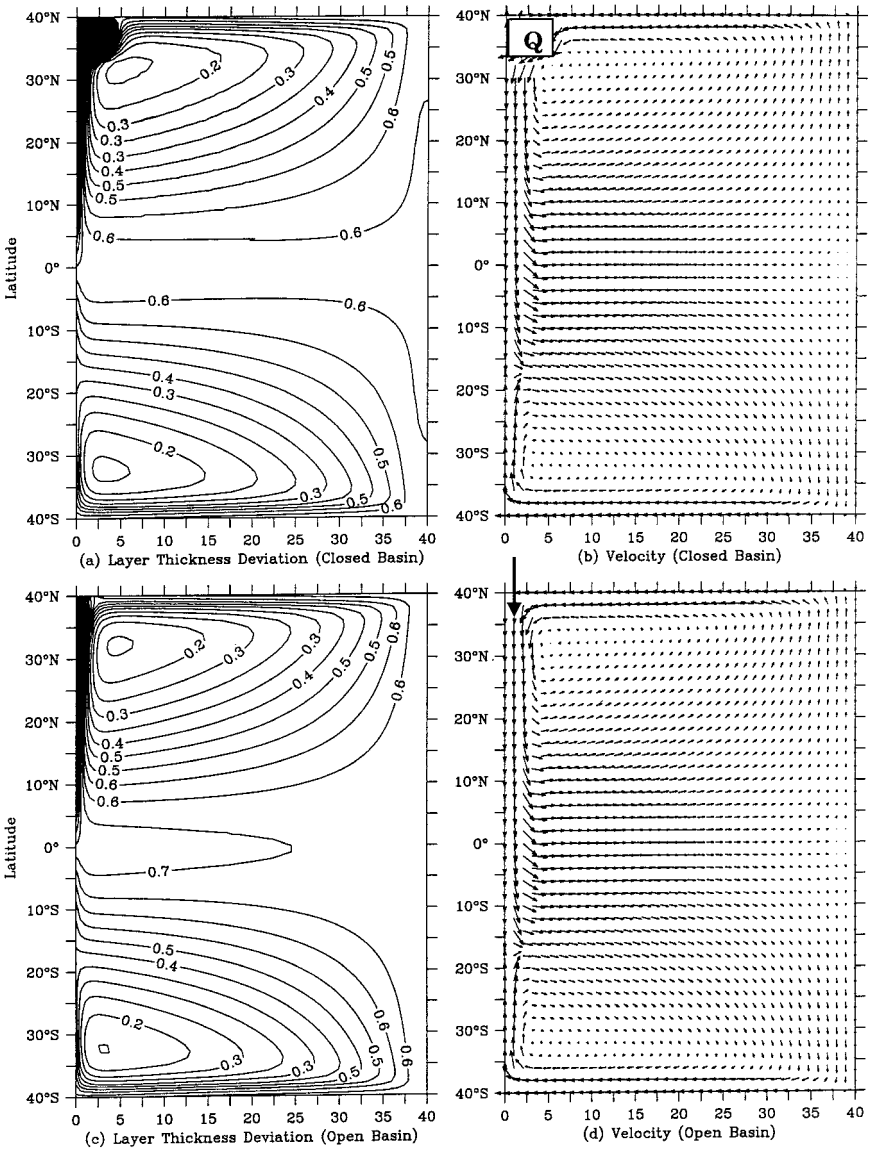

Figure 3. The deviation of the layer thickness and the circulation for the cases with water-mass sources being located in the northwestern corner. The results from these two experiments look very similar. The main difference is a strong and highly localized, recirculation in the closed basin case. This recirculation appears to be much weaker in (b) than what it really is. The magnitude of its associated boundary current is shown is Figure 4a (dashed line).

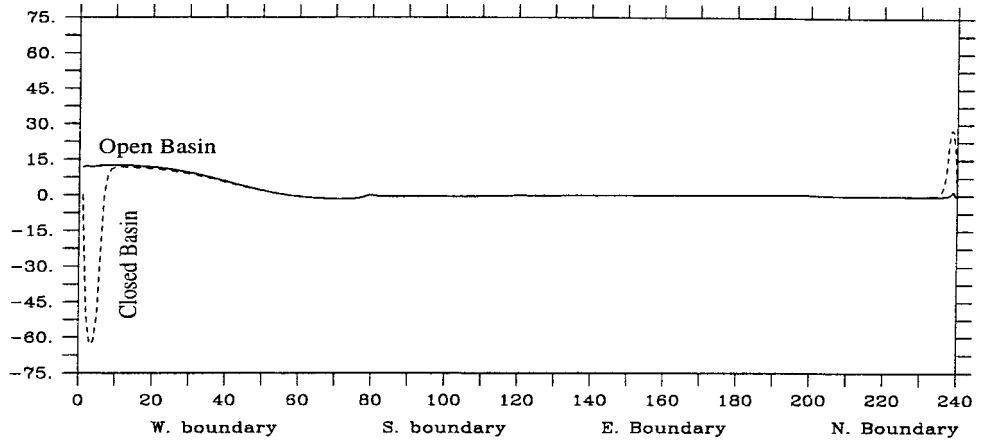

(a) The velocity along the boundary.

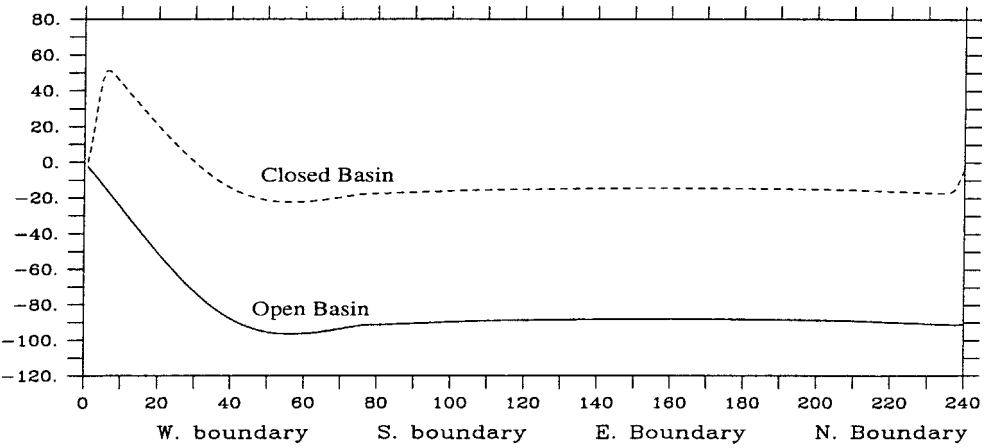

(b) The accumulated frictional vorticity production F(s).

Figure 4. The same as Figure 2 except for the experiments shown in Figure 3. Note that the major difference in boundary currents occurs only near the northwestern corner where the water-mass sources were introduced, but it results in the very different accumulated frictional vorticity production as shown in the lower panel.

the western boundary is about 60 $m^2\ s^{-1}$. In the parallel 'open-basin' experiment the water mass is supplied by an inflow through the northern boundary, Figure 3(c)–(d). The western boundary current is southward in regions north of 15S. The along-boundary velocity is shown in Figure 4(a) (solid line for the open basin). Comparing these two cases, the main difference in the flow field is localized to the area where the water mass is introduced (the difference of the boundary currents in these two cases appears to be small in Figure 3(b) and Figure 3(d) because the vector length was truncated in the plots; it is more evident in Figure 4(a) where the magnitude of velocity along the boundary is shown.) Away from that, both show that the interior circulation is in very good agreement with Stommel-Arons theory. Figure 4(b) shows $F(s)$ for both cases (solid line for the open basin and dashed line for the closed basin). The total frictional PV production ($F(s = 240°)$) is about $-2\ m^2\ s^{-1}$ for the closed basin and about $-91\ m^2\ s^{-1}$ for the open basin, which are close to the expected values of $0\ m^2\ s^{-1}$ and $-91.5\ m^2\ s^{-1}$.

It is interesting to note, however, that the distinction of the interior circulation between the two parallel cases, the open-basin and the closed-basin, is more visible when the water-mass source is located farther away from the western boundary, such as those shown in Figure 1, as compared with western source shown in Figure 3. A recirculation, known as the β-plume (see Pedlosky, 1996), develops to the west of an interior downwelling source (such as the one shown in Figure 1(b)). In the first pair of experiments, the water-mass source is located in the eastern basin and so the β-plume extends across the whole basin. When the source is moved close to the western boundary, shown in Figure 3(a)–(b), a very intense recirculation develops near the western boundary, though the vast majority of the basin is unaffected. It is important to point out that this recirculation, though localized, is an essential element of the global PV balance (15), as shown by Figure 4(b).

ii. Eastern source. Next, we consider a case in which the water-mass source is near the eastern boundary at the middle latitude. In the 'closed-basin' model, Q is distributed uniformly over an area $34° \leq \phi \leq 38°$ and $18N \leq \theta \leq 22N$, Figure 5(a)–(b). Due to vortex squashing the flow turns southward where the water mass is injected. A zonal current then transports mass eastward. Upon reaching the western boundary, the current is then bifurcated at about 15N. The northward branch feeds water mass into an eastward flow toward the water-mass source near the eastern boundary, and forms a recirculation gyre between 15N and 30N. The frictional PV production along the western boundary is positive north of 15N where the boundary current is northward and negative to the south of 15N where the current is southward. Therefore, the bifurcation of the western boundary current at 15N appears to result from the need to satisfy the constraint (15). In the 'open-basin' model, the same amount of water-mass flux is specified as an inflow at the eastern boundary between 19N and 21N. The water mass, after entering the basin, turns northward and converges to the northern boundary (Fig. 5(c)–(d)). A westward boundary current is formed along the northern boundary due to this convergence. Meanwhile, the western boundary current is strong and southward in the entire northern hemisphere. This

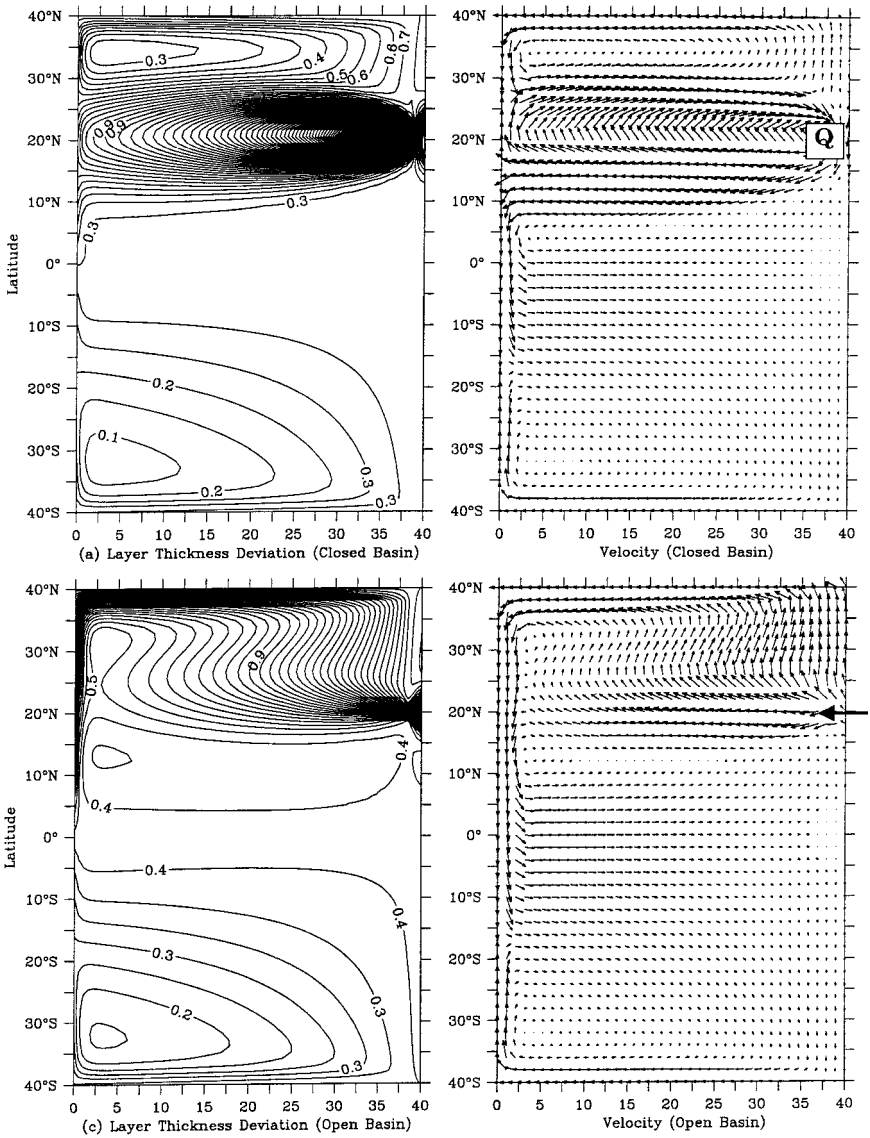

Figure 5. The same as Figure 1 except that the water-mass source/inflow is moved to the mid-latitude near the eastern boundary. The downwelling source drives a β-plume recirculation whose associated northward western boundary current ensures that the line integral of the boundary current vanishes and (15) is satisfied. The circulation is cyclonic in the open-basin case as required by (14).

circulation pattern, both in the interior and along boundaries, is considerably different from the 'closed-basin' model.

iii. Equatorial source. Finally, we consider a case where the water-mass source is placed at the equator. Since the planetary *PV* is now zero, the *PV* inflow term vanishes, and thus, the *PV* constraint in the open basin (14) becomes identical to that in the closed basin (15). Except for some small differences in the velocity field near the water-mass source, the circulations in these two experiments are nearly identical, as was expected from the *PV* constraint (compare Figs. 6(a)–(b) and 6(c)–(d)).

In the Stommel-Arons model the upwelling is specified *a priori* as a broad-scale and uniform vertical velocity which also serves as the sink for a localized water-mass source. In the present model, the upwelling is linked to the model circulation as a mass damping term, i.e., $-\kappa h$ in (3). How this term is specified does not affect the *PV* integral (14) and (15) since the upwelling does not contribute to the total *PV* budget (the cancelation of A_1 and A_2 in (7)), but does affect some aspects of the circulation. Specifically, this upwelling (or water-mass sink) term drives the interior Sverdrup circulation and with it the specification of where and how the water-mass is introduced to the abyssal layer. Thus, mass damping does influence the overall circulation pattern. Our emphasis here, however, is on the impact of regional source/sinks due to marginal sea outflow or localized convection.

4. Some topographic effects on PV inflow/outflow

Water-mass exchange between two basins often takes place over a sill as occurs in marginal-sea outflows. The layer thickness of an overflowing water mass may undergo substantial contraction when it flows over a sill. In that case, the *PV* inflow/outflow through an opening, represented by the term on the left-hand-side in (14), depends not only on the planetary vorticity f_i, but also on the thickness, H_i, of the inflow/outflow water layer. To see the consequences, we have used a nonlinear version of (1)–(3) in a smaller model domain which spans 20° in longitude and extends from 40N to 60N. The model resolution is 0.1° in both longitude and latitude. In the following experiments, the model is driven by a zonal inflow (1 Sv) at the western boundary at 50N and a zonal outflow (1 Sv) at the same latitude in the eastern boundary. The inflow and outflow are specified uniformly over 10 grid point from 49.5N to 50.5N as boundary conditions for u. Because of this slug flow representation, neither the inflow nor the outflow transports relative *PV* according to the discussion in Sections 2 and 3. The *PV* constraint (14) then becomes:

$$Qf\left(\frac{1}{H_o}-\frac{1}{H_{in}}\right)=-\lambda \oint_C (\mathbf{u}_h\cdot\mathbf{l})\,ds \tag{17}$$

where H_o and H_{in} are layer thickness at the outflow and inflow.

In the first null experiment, both H_o and H_{in} are chosen to be 2500 m (Fig. 7(c)), and so the left-hand-side term in (17) vanishes. The model result shows that a zonal current transports the inflow water directly across the basin to supply the outflow (Fig. 8(c)). The

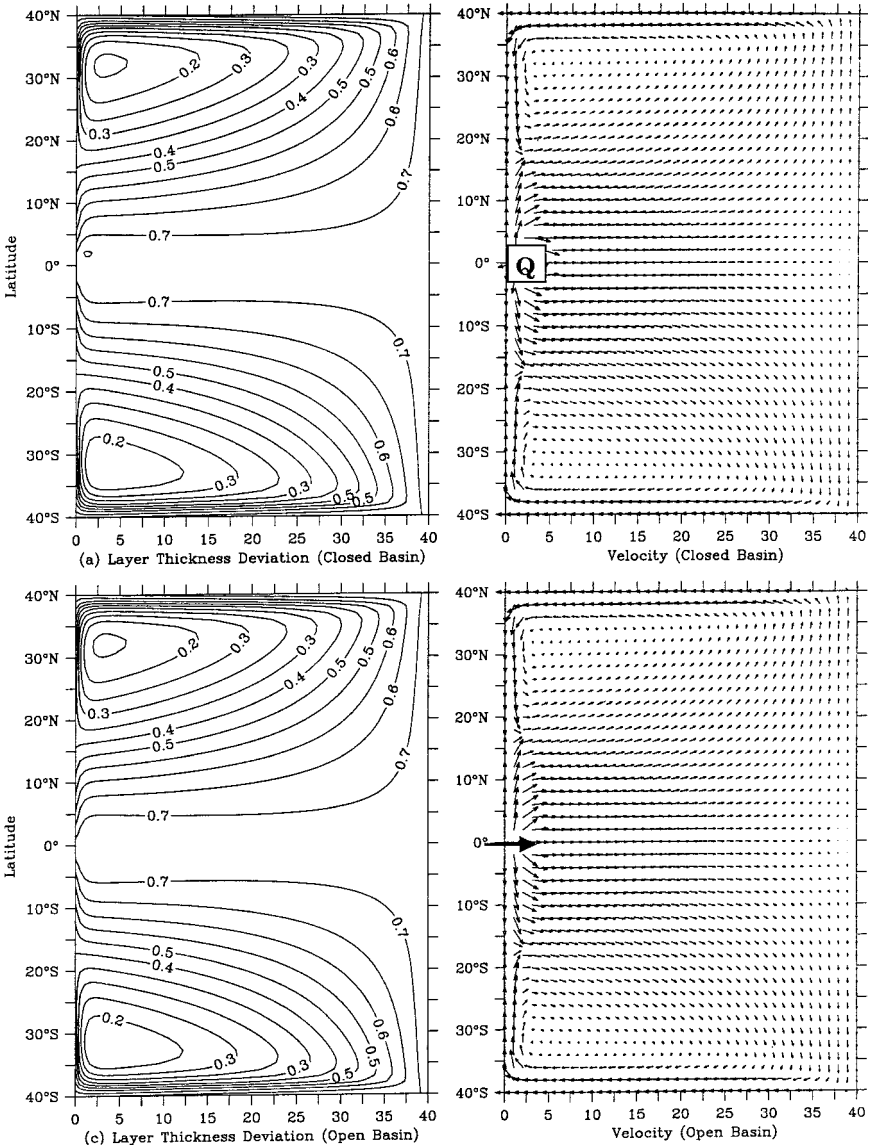

Figure 6. The model results for equatorial sources of water mass. The flow fields for the open-basin and the closed-basin cases are nearly identical because $f = 0$ at the equator and thus the PV constraint (14) for the open basin becomes the same as (15), the constraint for the closed-basin model.

western boundary current, which is very weak, bifurcates evenly at the inflow latitude so that the line integral of current around the basin is zero, giving zero net frictional torque.

In the following four experiments we vary the bottom depth with longitude so that $H_{out} \neq H_{in}$ and so that there is a significant topographic effect in the PV balance. As a first

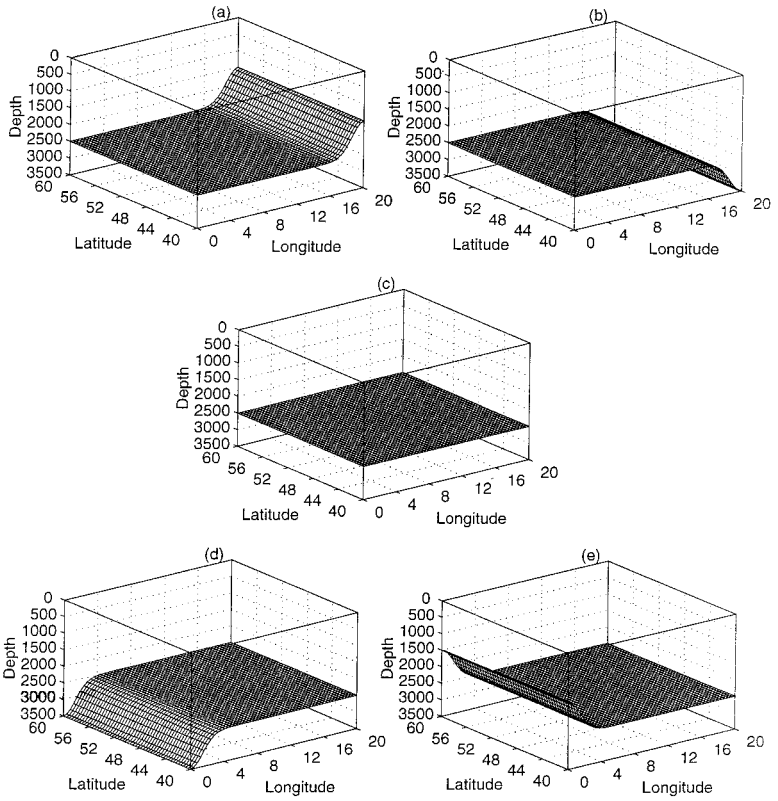

Figure 7. Five different topographic configurations used in the model experiments. In all these cases, the inflow takes place at the western boundary between 49.5N and 50.5N and outflow is at the same latitude at the eastern boundary.

example, imagine that the bottom depth is made shallower along the outflow (eastern) side of the basin while leaving the central and western regions flat (see Fig. 7(a) but try to avoid the circulation diagram, Figure 8, until you have had a chance to guess or infer the circulation). From (17) we would expect that there must be a positive PV source associated with this topography and the combined inflow and outflow since the PV export is greater than the PV import ($H_{out} \leq H_{in}$). In steady state, the net frictional torque must then be positive to achieve a steady PV balance, and thus the associated boundary currents must have a negative line integral around the basin, i.e., the sense of the boundary current flow expected from the PV balance must be anticyclonic or clockwise. This sense of the boundary circulation is just contrary to (our, naive, evidently) expectation that the inflow would turn right or southward upon entering the basin. In the event, the PV balance-inferred clockwise circulation is, indeed, just what the model produces (cf., Fig. 8(a)). If the sense of the topographic variation is reversed (shallower inflow than outflow) then the

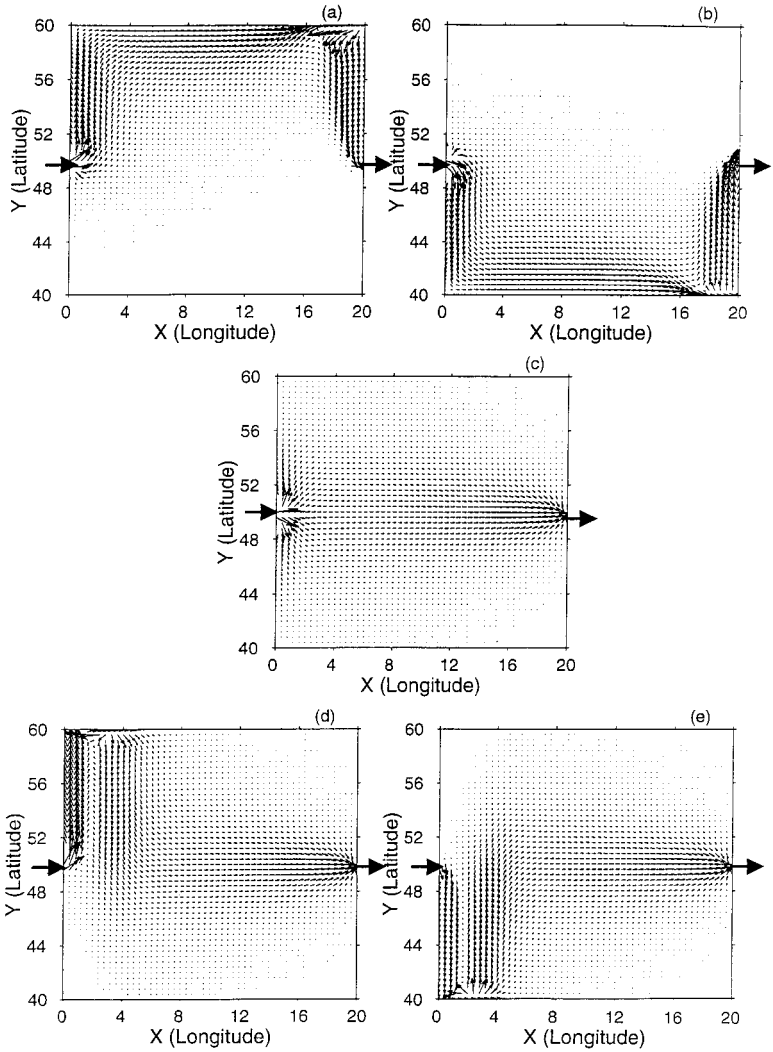

Figure 8. The model flow fields using five types of topography shown in Figure 8. Note that the sense of the circulation depends on the depth difference of inflow and outflow. If the inflow occurs at a deeper opening than that for the outflow, such as in (a) and (d), the sense of circulation will be anticyclonic, and vice versa for the opposite cases. These results can be explained in terms of the *PV* constraint (17).

PV source associated with the inflow and outflow is also reversed, as is the boundary circulation (Figs. 7(b) and 8(b)).

To carry this a bit further, we can impose the topographic variation over the western side of the basin, while leaving the eastern and central regions flat. Say that the western (inflow) side of the basin is made deeper (Fig. 7(d), then the *PV* source associated with the inflow

and outflow is nearly the same as in the first example, Fig. 7(a), 8(a)). Hence, we would expect a clockwise boundary circulation. That is what we find (Fig. 8(d)) but with an important difference from the example in Figure 7(a) and 8(a). In this instance the southward flow needed to get water back down to the latitude of the outflow occurs along the sloping topography of the western basin rather than along the eastern side of the basin as in 7(a) and 8(a). Since the southward flow occurs within the interior, it makes no contribution to the net torque or the *PV* balance. Thus the northward boundary current of 8(d) has the entire burden of the frictional torque, and is roughly twice as intense as is the corresponding northward boundary current of 8(a).

The preceding experiments showed that the sense of basin-scale circulation, particularly the boundary layer currents, is controlled by the *PV* of the source. As far as the *PV* budget is concerned, outflows and inflows may have very similar effects. The major premise for using (17) as the *PV* constraint for the basin circulation is that the transport of relative vorticity is negligible compared with that of planetary vorticity. Little is known about the relative *PV* for major outflows in the real ocean, although it has been suggested that ζ is about one order of magnitude smaller than f in the deep-water flow through the Faroe Bank Channel (Borenäs and Lundberg, 1988; Saunders, 1990). If, however, the relative vorticity of inflow or outflow is comparable with f, such as that predicted by the zero *PV* theory for marginal-sea overflow (Whitehead *et al.,* 1974), then the basin circulation would be sensitive to the ζ distribution at the inflow and outflow.[2]

5. Summary

We have studied a highly-idealized abyssal circulation produced by specified mass sources. Our principal analysis tool has been the basin-wide *PV* budget, which gives considerable insight into the form of the boundary currents, especially. We have shown that a downwelling source represents zero net production of *PV*. Thus, in a steady circulation driven solely by such a source, the basin-wide production of *PV* by frictional processes must also be zero. The boundary current that transports water away from a downwelling, polar source must have at least a small region of intense, reversed flow somewhere along the boundary. In our experiments, these regions were found along the northern boundary and close to the source. By contrast, if the source comes through the side of the ocean model, as if due to a marginal sea overflow, then the source carries a net *PV* flux that is

2. We did a series of experiments similar to that shown in Fig. 1(c)–(d) but with inflow ζ set. To do this, a southward inflow was injected in the northern corner and in contact with the (free slip) eastern wall. In an experiment, the relative vorticity ζ is specified as $-f$, so that it cancels exactly the planetary vorticity; i.e., $f + \zeta = 0$, then there is no *PV* transported into the basin. The basin circulation has some notable differences as compared with the case of $\zeta = 0$ (e.g., Fig. 1(c)–(d)). The incoming current continues southward along the eastern boundary instead of heading toward the westward boundary directly along the northern boundary as in the previous case. This eastern boundary current feeds a northward interior flow governed by the Sverdrup dynamics (upwelling forces a poleward interior flow). The interior flow converges toward the northern boundary and forms a boundary current along the northern boundary which subsequently continues southward as the western boundary current. Because of this very strong southward eastern boundary current, the velocity integral along the boundary vanishes as required by the *PV* constraint.

equal to the inflow transport times $(f + \zeta)/H$. This PV source must be balanced by frictional torque in steady state, and in these calculations this occurs by a monotonic flow away from the source and along the northern and western boundary. This latter pattern, which supplies the necessary negative torque to balance the positive PV influx through the side, is thus a good deal simpler than the 'zero torque' pattern that occurs in association with a downwelling source. It also matches better our intuition regarding the real pattern of boundary currents in the ocean, but we cannot say that one or the other pattern is supported better by oceanic observations. The interior circulation is not greatly different between these two cases, and is much like the Stommel-Arons result. We have also conducted some experiments to illustrate the potential impacts of topography near inflow/outflow regions on the PV budget. Flows between two basins often occur over sills where the overflow layer may be compressed significantly due to the topography. The change of layer thickness can affect significantly the PV flux if the transport of the relative PV is small, and thus control the dissipation requirement in the upstream (and also in the downstream) basin. The numerical model showed that the flow patterns can be drastically altered by merely changing the bathymetry near the inflow or outflow. These results, though a little surprising, are consistent with the PV constraint as defined by (17).

The results from all experiments show that the sense of the basin-scale circulation (particularly the boundary currents) is largely determined by the net PV budget associated with the inflow and outflow. For a source-sink driven steady circulation, the constraint that the net PV flow must be balanced by the frictional PV production exerts a kind of PV control over the circulation in the ocean basin.

To apply these results to an interpretation of the real ocean would require a leap that we are not prepared to attempt, given the highly idealized character of these experiments, and given our lack of confidence in the frictional parameterizations. We can say that the details of convection are of some importance in numerical ocean models that seek to describe the deep circulation. Consequently, some effort toward modeling convection and deep water sources in a realistic way appears to be warranted.

Acknowledgments. We thank Dr. Joe Pedlosky for many helpful comments on a draft manuscript and Drs. Rui Xin Huang, Mike Spall, Larry Pratt, Karl Helfrich and Alan Faller for their constructive discussions of this problem. This study was supported by NSF grant number OCE-9616951. This is Woods Hole Oceanographic Institution contribution number 9616.

REFERENCES

Borenäs and Lundberg. 1988. On the deep-water flow through the Faroe Bank Channel. J. Geophys. Res., *93,* 1281–1292.

Kawase, M. 1987. Establishment of deep ocean circulation driven by deep-water production. J. Phys. Oceanogr., *17,* 2294–2317.

Pedlosky, J. 1979. Geophysical Fluid Dynamics, Springer-Verlag, Berlin, 624 pp.

—— 1996. Ocean Circulation Theory, Springer-Verlag, Berlin, 543 pp.

Pratt, L. J. 1997. Hydraulically drained flows in rotating basins. Part II: Steady flow. J. Phys. Oceanogr., *27,* 2522–2535.

Price, J. F. and M. O. Baringer. 1994. Outflows and deep water production by marginal seas. Prog. Oceanogr., *33,* 161–200.

Rhines, P. 1983. Lectures in geophysical fluid dynamics. Lectures in Appl. Math., *20,* 3–58.

Rhines, P. and P. MacCready. 1989. Boundary control over the large-scale circulation, *in* Parameterization of Small-Scale Processes, The Proceedings of Hawaii Winter Workshop, University of Hawaii at Monoa, January 17–20, 75–97.

Saunders, P. M. 1990. Cold outflow from the Faroe Bank Channel. J. Phys. Oceanogr., *20,* 29–43.

Stommel, H. 1958. The abyssal circulation. Deep-Sea Res., *5,* 80–82.

Stommel, H. and A. B. Arons. 1960a. On the abyssal circulation of the world ocean. I. Stationary planetary flow patterns on a sphere. Deep-Sea Res., *6,* 140–154.

—— 1960b. On the abyssal circulation of the world ocean. II. An idealized model of the circulation pattern and amplitude in oceanic basins. Deep-Sea Res., *6,* 217–233.

Warren, B. A. 1981. Deep circulation of the World Ocean, *in* Evolution of Physical Oceanography, B. A. Warren and C. Wunsch, eds., MIT Press, Cambridge, MA.

Whitehead, J. A., A. Leetmaa, and R. A. Knox. 1974. Rotating hydraulics of strait and sill flows. Geophys. Fluid Dyn., *6,* 101–125.

Yang, J. and J. F. Price. 2000. Modeling the thermohaline circulation: Some effects of marginal sea overflows. manuscript.

Received: *8 November, 1999;* revised: *5 July, 2000.*